SOILS AND FOUNDATIONS Vol. 45, No. 2, 167-180, Apr. 2005
Japanese Geotechnical Society

GROUND DENSIFICATION DUE TO SAND COMPACTION PILES

MÁRCIO M. FARIAS[i], TERUO NAKAI[iii], HOSSAIN M. SHAHIN[iv], DORIVAL M. PEDROSO[ii], PAULA G. O. PASSOS[ii] and MASAYA HINOKIO[v]

ABSTRACT

The geotechnical properties of granular soils can be improved using compaction piles. However, the compaction effect and the extent of the densification are not yet clear. Well controlled in situ tests are necessary to investigate this problem. Further insight about the densification process can also be gained by performing numerical analysis using a constitutive model that takes into account the effect of density and confining pressure on the behavior of soils. This paper presents numerical analyses in which a recently proposed model, named *subloading* t_{ij}, is used to simulate these effects. The construction process of sand compaction piles involves two stages: the metal casing driving and the sand pile compaction. The process is simulated sequentially and the relative influence of each stage is quantified for different initial ground density conditions. The extent and effectiveness of the densification are also quantified. The results of these predictions are qualitatively compared with the results of field tests carried out before and after the execution of compaction piles in an artificial loose sand deposit. There is good overall agreement between the numerical predictions and the test results, showing that a combination of these two investigation approaches is a way forward to better understanding the densification process. However, this can only be achieved if the constitutive model can properly account for the change in soil behavior with densification.

Key words: compaction, constitutive equation of soil, density, finite element method, in-situ test, pile driving, sand compaction piles (**IGC:** C3/D9/E13)

INTRODUCTION

Several techniques for improving the geotechnical characteristics of foundation areas have been developed with the main objective of reducing the costs related to civil engineering constructions. Some techniques are more suitable for cohesive soils, while others are specific for cohesionless soils. For sandy granular soils in particular, sand-gravel compaction piles are widely used in many parts of the world.

Sand-gravel compaction piles are often used to avoid liquefaction in areas of high seismicity, such as in Japan (Ichimoto and Suematsu, 1981; Asaoka et al., 1994; Okamura et al., 2003). Also in several cities in the northeastern region of Brazil, where large deposits of loose granular layers are quite common, these piles have been successfully used to enhance the bearing capacity of the ground. Increases in load capacity up to five folds have been achieved and buildings with 20 to 30 stories have been constructed using shallow block foundation over the soil improved with this technique (Gusmão Filho, 1995).

The general aspects of the execution of sand piles and the soil improvement control are currently done in an empirical manner. It has been observed that the densification process is more effective for looser grounds. It is also believed that soil improvement originates from two different sources: a) Volume change due to the introduction of the metallic casing with a closed end; and b) Further densification due to the introduction and compaction of the sand piles as the metallic casing is pulled out. However, the relative importance of these effects, as well as the extent of the densification around the piles, is not yet clear. Some indication may be obtained in field by means of extensive in-situ testing, but further insight on the densification process could be gained using advanced numerical analysis. The main difficulty in this case is that most constitutive models available use different parameters for different soil densities and confining pressures.

The subloading t_{ij} model, recently proposed by Nakai and Hinokio (2003, 2004), takes into consideration the influence of density and confining pressures with a single set of soil parameters. Farias et al. (2003) used this model

i) Professor of Geotechnics, University of Brasilia, Brasilia-DF, Brazil (muniz@unb.br).
ii) PhD Students, ditto.
iii) Professor of Geotechnics, Nagoya Institute of Technology, Gokiso-cho, Showa-ku, Nagoya 466-8555, Japan.
iv) PhD Student, ditto.
v) Research Associate, ditto.
The manuscript for this paper was received for review on March 3, 2004; approved on March 11, 2005.
Written discussions on this paper should be submitted before November 1, 2005 to the Japanese Geotechnical Society, 4-38-2, Sengoku, Bunkyo-ku, Tokyo 112-0011, Japan. Upon request the closing date may be extended one month.

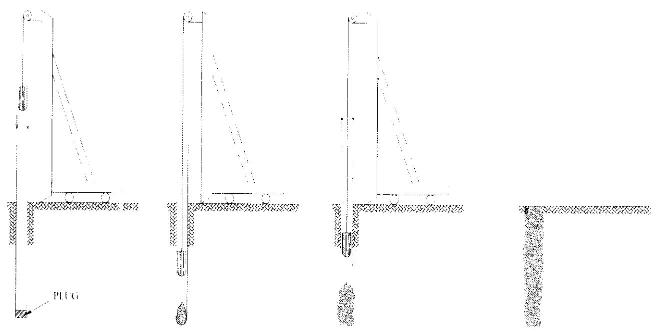

Fig. 1. Sand pile construction process (Modified from Gusmão Filho, 1995)

to study the densification process during the construction of sand piles in a predictive manner, using a typical geometry of current practice and assuming the parameters of Toyoura sand. More recently, the results of in-situ tests carried out under well controlled conditions have been made available (Passos et al., 2004). Results of these tests are used here to validate the numerical results.

SAND-GRAVEL COMPACTION PILES

The construction process of sand-gravel compaction piles generally used in Brazil consists initially of the introduction of a metal casing with a closed end into the ground. The process is similar to the execution of Franki piles (Neely, 1990), and the casing end is closed with a cement plug. When the casing reaches the desired depth, the cement plug is broken (fixing the casing and hammering the plug) and a mixture of sand and gravel is introduced into the case. This material is compacted dynamically, using a free falling hammer. As the sand-gravel pile is compacted, the metal casing is gradually pulled out. The process continues until the pile reaches the ground surface as illustrated in Fig. 1.

The common practice of sand compaction piles in Brazil is described in Gusmão Filho (1995). The mixture used for the pile is generally composed of three portions of sand to one portion of gravel in volume. The basic equipment for improving shallow ground deposits (up to 5 m) consists of a tripod and a hammer weighting 13 to 15 kN, with a fall height of 3 m. The usual pile casing diameter is 300 mm. After driving the metal casing and breaking the plug, the metal tube is filled with sand-gravel in sequential stages with heights corresponding to about 3 diameters of the pile. The corresponding compaction energy is close to that of the Normal Proctor laboratory test. Soil improvement is performed with the construction of sand compaction piles in a square or triangular grid spaced of 2 or 3 pile diameters between pile centers.

Farias et al. (2003) simulated numerically a typical configuration described above for different initial ground density conditions, using the parameters of Toyoura sand for the new subloading t_{ij} model of Nakai and Hinokio (2003, 2004). This model is briefly described in the next section.

BRIEF DESCRIPTION OF SUBLOADING t_{ij} MODEL

The subloading t_{ij} constitutive model (Nakai and Hinokio, 2003, 2004), despite using a small number of parameters, can describe the following important features of soil behavior: a) Intermediate principal stress effect on the deformation and strength of soils; b) Dependence between stress paths and the direction of plastic flow; and c) Influence of density and confining pressure on the deformation and strength of soils.

The modified stress tensor t_{ij} (Nakai and Mihara, 1984) is the core of the model and it is based on the concepts of the Spatially Mobilized Plane (SMP) (Matsuoka and Nakai, 1974) and its modified version SMP* (Nakai and Matsuoka, 1983). A second order tensor, represented by a_{ij}, is defined in such a way that the principal values of a_{ij} are the three components of the vector normal to the SMP, and the principal directions of a_{ij} are co-axial with the principal stress directions. Tensor t_{ij} is defined as:

$$t_{ij}=a_{ik}\sigma_{kj} \tag{1}$$

The normal and shear invariants (t_N and t_S) of tensor t_{ij}, represent the normal and shear stresses acting on the SMP (σ_{SMP} and τ_{SMP}). Tensor t_{ij} accounts for the influence of the intermediate stresses on the deformation and strength of soils. From a mathematical point of view, t_{ij} implies in a mapping of the conventional stresses to a modified stress space. The definition of an associated flow rule in this new space results in a kind of non-associated flow rule in the conventional stress space without requiring the explicit definition of a different plastic potential function and without introducing any extra model parameters. Several publications confirm the potential capabilities of models based on t_{ij} concept when they compared it to conventional models (Matsuoka and Nakai, 1986; Nakai, 1989; Chowdhury and Nakai, 1998; Pedroso, 2002; Pedroso and Farias, 2003).

In order to represent the interdependence between stress paths and the direction of plastic strain increment, the plastic strain increment is divided into two components: one satisfying the associate flow rule in the space of the modified stress t_{ij} and the other, named isotropic compression component, is given by a function of the rate between the normal invariant increment and the size of the subloading yield surface. This last component is computed only when the increment of normal invariant t_N is positive.

The influence of density on the deformation and strength of soils is taken into account by defining two surfaces, as illustrated in Fig. 2: one is the subloading surface and the other is the normal yield surface (Dafalias and Popov, 1975; Hashiguchi, 1980). The current stress point, denoted by P in Fig. 2, always lies on the inner subloading surface. The outer normal surface works as a loading memory and allows to quantify how dense or

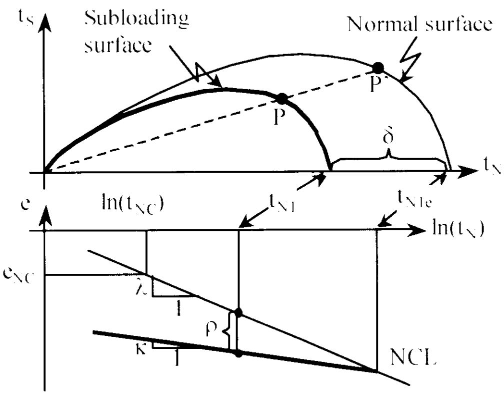

Fig. 2. Shape of subloading and normal yield surfaces: Definition of ρ

overconsolidated the point is. Upon unloading, the normal yield surface remains stationary, while the subloading surface shrinks and only elastic strains occur. During reloading, elastic and plastic strains take place and both the surfaces expand. However, the subloading surface expands at a faster rate and the current stress approaches its mirror or image stress P' as the point becomes normally consolidated. This feature avoids the typical discontinuity in the hardening evolution, which marks the transition between elastic and elasto-plastic strains in models with a single yield surface. It also allows the simulation of hysteresis during cyclic loading.

The sizes of the normal and subloading yield surfaces are measured by the mean stress values at the tip of these surfaces, denoted, respectively, by t_{N1e} and t_{N1} in the modified stress space depicted in the upper part of Fig. 2. The difference in size between these two surfaces $\delta = t_{N1e} - t_{N1}$ is a stress-like hardening variable that gives a measure of how much overconsolidated is the current stress point. Assuming a linear relation between the void ratio and the natural logarithm of the mean stress, the "distance" between the normal and subloading yield surfaces may be expressed in terms of an alternative variable (ρ), or its value divided by $(1+e_0)$ in order to have a strain-like hardening variable, defined as:

$$\frac{\rho}{1+e_0} = \frac{\lambda-\kappa}{1+e_0} \ln\left(\frac{t_{N1e}}{t_{N1}}\right) \quad \text{or} \quad \frac{\rho}{1+e_0} = C^p \ln\left(\frac{t_{N1e}}{t_{N1}}\right) \tag{2}$$

where λ and κ are material parameters, related to the compression and swelling indices, and $C^p = (\lambda-\kappa)/(1+e_0)$ is a measure of plastic volumetric compliance.

It can be seen from Fig. 2 that variable ρ gives a numerical measure of pre-consolidation, in terms of plastic void ratio difference between the present state and the loosest density state (Normal Consolidation Line–NCL) at the same stress. This variable can be considered an additional internal hardening variable of the model for which an evolution law must be defined. This law should be such that the two yield surfaces approach each other as the material becomes normally consolidated. Nakai and Hinokio (2003, 2004) suggested that the evolution of $\rho/(1+e_0)$, which represents the change in density during plastic deformation, depends only on its present value and on the value of the confining pressure measured by the invariant t_N, according to a general expression like:

$$d\left(\frac{\rho}{1+e_0}\right) = \Lambda \cdot L(\rho, t_N) \tag{3}$$

in which Λ is the plastic multiplier and $L(\rho, t_N)$ is a function that is formulated in such a way as to explain the observed experimental behavior of soils in either normally consolidated or overconsolidated states. From the consistency condition ($df=0$), which is imposed on the subloading yield surface, the plastic multiplier can be obtained as:

$$\Lambda = \frac{\dfrac{\partial f}{\partial \sigma_{ij}} d\sigma_{ij}}{\dfrac{1}{C^p}\left(\dfrac{\partial f}{\partial t_{kk}} - L(\rho, t_N)\right)} \tag{4}$$

The formulation of $L(\rho, t_N)$ should take the following points into consideration (Nakai and Hinokio, 2004): (i) whenever plastic deformation occurs, Λ is positive; (ii) the overconsolidated state moves toward the normally consolidated state with development of plastic deformation, so the increment $d\rho/(1+e_0)$ should be negative; (iii) Equation (4) should become equal to that of a normally consolidated state for $\rho=0$. In order to satisfy these conditions, the function $L(\rho, t_N)$ should be negative for $\rho>0$ and should vanish for $\rho=0$. The experimental results of laboratory tests under different stress paths and for different overconsolidation ratios show an unique relation between stresses ratio (q/p or t_S/t_N) and the deviatoric strains, regardless of mean stress values. Furthermore, the dimension of $L(\rho, t_N)$ in Eq. (4) should be the same as $\partial f/\partial t_{kk}$, i.e., the inverse of stress. Therefore, $L(\rho, t_N)$ is defined as:

$$L(\rho, t_N) = -\frac{G(\rho)}{t_N} \tag{5}$$

in which $G(\rho)$ is a function of ρ that should satisfy the condition $G(0)=0$. Furthermore, the stiffness and strength of overconsolidated soils increase with density ρ. The denominator of Eq. (4) is related to the soil stiffness, and the relation between density and stiffness and peak strength is obtained when this denominator becomes zero. Therefore, besides the condition of $G(0)=0$, function $G(\rho)$ should be monotonically increasing. Any suitable function satisfying the above conditions may be chosen, but Nakai and Hinokio (2004) proposed a simple quadratic function given:

$$G(\rho) = a \cdot \rho^2 \tag{6}$$

in which a, is the only additional model parameter with respect to t_{ij}-clay model (Nakai and Matsuoka, 1986). Parameter a controls the rate of convergence between the subloading and normal yield surfaces. The adoption of Eqs. (5) and (6) allows subloading t_{ij} model to account for the influence of the confining pressure (via t_N) and the density state (ρ) on the behavior of soils, using a unified set of material parameters.

Based on the unique stress ratio-dilatancy curve,

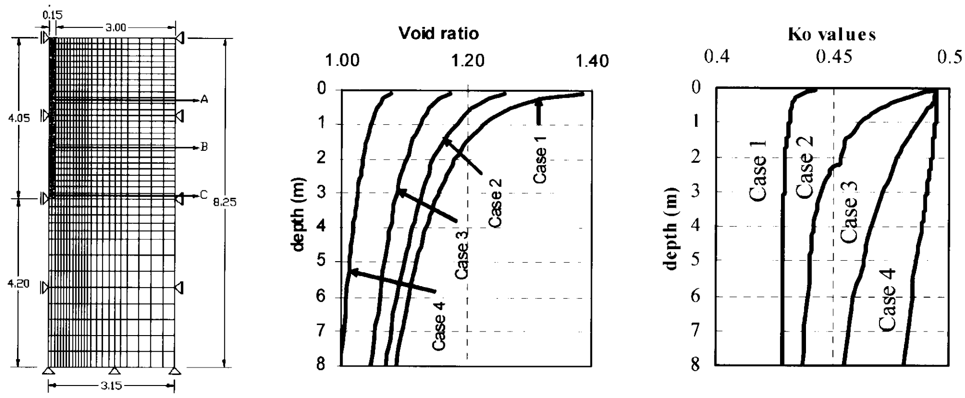

(a) F.E. mesh (units in m.) (b) Initial void ratio (c) Ko profiles

Fig. 3. Geometry, mesh and initial state for the problem analyzed

Chowdhury and Nakai (1998) deduced the following expression for the yield function:

$$f(t_N, t_S, t_{N1}) = \ln\left(\frac{t_N}{t_{N1}}\right) + \frac{1}{\beta}\left(\frac{t_S}{M^* t_N}\right)^\beta \tag{7}$$

in which M^* and β are model parameters, and t_{N1} is the stress-like hardening variable that measures the size of the yield surface. Parameter β controls the shape of the yield surface and M^* is related to the friction angle (ϕ_{CS}) or to the ratio between the major and minor principal stresses at the critical state under triaxial compression (R_{CS}) by the following expression:

$$M^* = (X_{CS}^\beta + X_{CS}^{\beta-1} Y_{CS})^{1/\beta} \tag{8}$$

where

$$X_{CS} = \frac{\sqrt{2}}{3}\left(\sqrt{R_{CS}} - \frac{1}{\sqrt{R_{CS}}}\right) \tag{9}$$

$$Y_{CS} = \frac{1 - \sqrt{R_{CS}}}{\sqrt{2}(\sqrt{R_{CS}} + 0.5)} \tag{10}$$

and

$$R_{CS} = \left(\frac{\sigma_1}{\sigma_3}\right)_{CS(comp.)} = \frac{1 + \sin\phi_{CS(comp.)}}{1 - \sin\phi_{CS(comp.)}} = \tan^2\left(45° + \frac{\phi_{CS(comp.)}}{2}\right) \tag{11}$$

An expression similar to Eq. (7) may be written for the normal yield surface (F), using the mirror stresses (P′ in Fig. 2) and t_{N1c} instead of t_{N1} for the size of this surface. However, the normal yield surface is not required for the deduction of the stress-strain relation and it is linked to the subloading surface via the internal variable ρ.

NUMERICAL SIMULATION

Fully predictive numerical simulations of the densification process were carried out, considering one single pile and a typical configuration used in current practice (Farias et al., 2003). These predictions can be considered as class A, according to the definition of Lambe (1973). The adopted mesh takes advantage of the axisymmetry of the problem and is shown in Fig. 3(a). Isoparametric quadrilateral elements with four nodes and 2×2 Gaussian integration were used. The sand pile is 4.05 m deep and its diameter is equal to 30 cm. The ground extends to 8.25 m in depth and 3.15 m laterally. Both vertical faces of the mesh are free in the vertical direction and the bottom face is kept fixed.

Table 1. Sub-loading t_{ij}-model parameters for Toyoura sand (Nakai and Hinokio, 2003)

λ	κ	e_{NC}	R_{CS} (ϕ_{cs})	β	ν	a	
						a_{AF}	a_{IC}
0.070	0.0045	1.1	3.2 (31.6°)	2.0	0.2	30	500

The sandy ground is simulated using the parameters of Toyoura sand shown in Table 1. Geostatic stresses are initially generated, applying the soil unit weight ($\gamma = 15.8$ kN/m^3) under one-dimensional (vertical) strain state from a nearly null stress condition in several small increments. Initial values of uniform void ratio, ranging from 1.1 to 1.5, were initially assigned to the unstressed ground. As the self weight was activated, different initial void ratio profiles were generated as indicated by cases 1 to 4 in Fig. 3(b). The initial ground of Case 1 is comparatively looser than that of Case 4. The ground density varies with depth, since void ratio decreases with increasing depth of the ground, as one would expect in practice. These initial values are not realistic for Toyoura sand deposits, although such high values may be found in many regions of the world with collapsible sand, silt or clay deposits. The high values of initial void ratio used here are justified only to emphasize the ability of the model in reproducing sand densification.

The initial geostatic stresses determined under one-dimensional strain conditions, as described above, generates coefficients of lateral stress at rest (K_0) which vary with depth and initial density state. Figure 3(c)

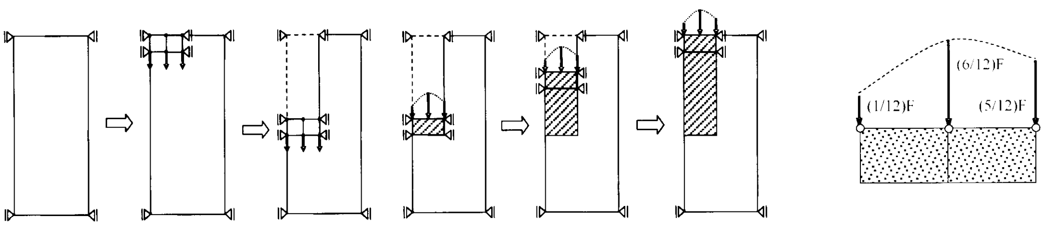

(a) Stage 1 – Casing driving (b) Stage 2 – Compaction (c) Details of load application

Fig. 4. Simulation procedure

shows the K_0 profiles and the values ranged from 0.42 to 0.48. Values of K_0 are higher at the surface and decrease with depth as the initial void ratio profile. However, K_0 values are higher for the initially denser states, such as Case 4.

The initial stresses, correspondent to the geostatic (self-weight) condition, are assigned to the ground in all numerical analyses. The sand pile construction analysis is performed in two stages, as illustrated in Fig. 4 and described in the following:

1st Stage: Casing Driving—The steps for the simulation of the metal casing driving are as follows:

1. Starting from the top of the ground in the region of the compaction pile, impose uniform vertical displacements to the nodes at the bottom of the casing, while keeping the nodes in the periphery fixed only in the horizontal direction. Displacement values are equal to the height of the elements and must be applied in several small steps;
2. Deactivate the elements inside the metal casing from the previous step;
3. Repeat 1 and 2 until the bottom is reached.

After driving the metal casing in the first stage, stresses, void ratios and density parameters of the constitutive model at all integration points are stored and then used as the initial conditions of the ground for the second stage of the analysis.

2nd Stage: Sand Pile Compaction—The compaction phase is simulated with the following steps:

1. Activate sequentially the elements inside the metal casing, starting from the bottom layer. This is achieved by re-creating elements and applying their self-weight in small steps;
2. Impose vertical forces at the top nodes of the layer with the values calculated according to the detail in Fig. 4(c) for the static simulation of the hammer load;
3. Set the previous force to zero, simulating the completion of the hammer load in this layer, and free the nodes at the casing bottom to allow for the casing withdrawal;
4. Repeat 1 to 3 until the top is reached.

The imposed load was 2.205 kN/radian for each layer, due to the axisymmetric condition. The total load for each layer is 13.85 kN acting over an area of 0.2826 m^2 or 49 kPa. The equivalent nodal forces under axisymmetric conditions are applied to nodes of each layer according to the detail in Fig. 4(c). The fractions of the total force applied to the central, intermediate and external nodes (1/12, 6/12 and 5/12, respectively) were computed considering that a load uniformly distributed over a sector of one radian, as used in axisymmetric finite element analysis, is equivalent to load with a triangular distribution over the same radius. The load was applied only once to each layer and then set equal to zero before the next layer is constructed.

A final comment should be added about two important aspects of the numerical simulation of the problem analyzed here: the consideration of large strains and the pile dynamic penetration effect. Metal casing installation certainly produces large strains in a localized area in the interface between the casing and the surrounding soil. Miyata et al. (2003), using the same finite element program and subloading t_{ij} model adopted in the present analyses, studied the formation of shear bands in clay specimens subjected to large deformations under two-dimensional stress conditions. The authors used both finite and infinitesimal strain theories to simulate shear tests with imposed strains in the order of 40%, which brought the specimens to the critical state condition. The results of both simulations are very close, although the shear band is more clearly identified in the simulations using large strain theory. Therefore the analyses carried out here adopt the small strain theory for the sake of simplicity.

As to the influence of dynamic effects during casing installation and the compaction of sand piles, the authors believe that they might play an important role, but this simulation is not possible with the present version of the program available. Despite the use of static loads in the present analyses, the authors believe that the overall qualitative observations should be valid as a whole.

NUMERICAL RESULTS AND DISCUSSIONS

Void Ratio Changes

The result of each calculation is represented by the relative change of the void ratio of the ground, which is one measure of ground densification. The relative change of void ratio is calculated according to the following simple formula:

$$\Delta e_{\mathrm{R}} = \frac{e_{\mathrm{i}} - e_{\mathrm{f}}}{e_{\mathrm{i}}} \times 100 \tag{12}$$

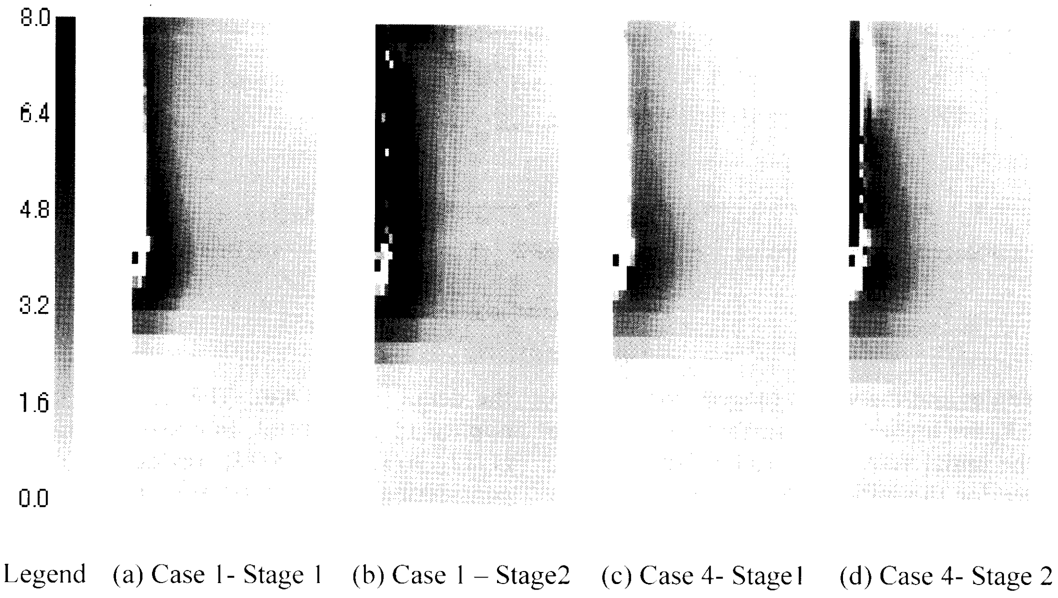

Fig. 5. Relative change of void ratio

where, Δe_R is the relative change of void ratio in percentage after completion of each stage, e_i is the void ratio at the geostatic condition given in Fig. 3(b) and e_f is the void ratio after completion of each stage. Any other suitable measure of densification could be adopted. The expression in Eq. (12) is similar to the change in relative density (D_r) divided by the initial value of D_r, however it does not need the definition of maximum and minimum void ratio values (e_{max} and e_{min}).

Figures 5(a)-(d) show the distributions of the relative change of void ratio in percentage for Case 1 and Case 4 at the end of each construction stage. All figures are drawn with the same scale, shown in the legend, so that results can be compared directly for different cases. It is seen in Figs. 5(a) and (c) that, after driving the metal casing, a significant portion of the ground is compacted to some extent, mainly at the bottom of the casing. Some elements alongside the pile border dilate at the end of the casing driving stage. These elements are initially loose and become compact as the metal casing tip approaches them. Then, due to their now higher density state they tend to dilate and expand due to further shearing as the metal casing is driven to its final depth.

During compaction of the sand pile (Stage 2) the ground undergoes further densification. Here, loads are applied in the vertical direction, and it is seen that the ground became dense in the horizontal direction as well. Intensity of the densification is higher near the sand pile and gradually decreases with distance from the center of the pile. From these figures it is seen that the intensity and extent of densification clearly depend on the initial density state of the ground. If the ground is initially very loose, it becomes denser after compaction; however, compaction is not effective in dense grounds and these soils might even dilate and become looser.

The effect of densification and its extent in each state can be better appreciated from Fig. 6. The figures show the void ratio distribution with depth at different distances from the pile centre, corresponding to 1.5, 3.0 and 5.0 pile diameters (D), for the looser Case 1. Figure 6(a) shows the values of void ratio at the end of Stage 1. Note the densification along the pile, but the most affected area at this stage is below the pile tip, up to a depth of about 5.6 m or roughly 5 (five) pile diameters, as also shown in Figs. 5(a)-(d). The effect and extent of densification after the construction of the pile is shown in Fig. 6(b). It can be seen that, during this stage, densification becomes more uniform along the pile, except for the upper part, where confinement is low.

Figure 7 summarizes the compaction effect at different stages on the vertical and on the horizontal directions. Figure 7(a) shows the relative change of void ratio with depth at the final configuration for the looser Case 1. The influence of densification reduces gradually with the distance from the pile and the relative void ratio reduction is less than to 2% at a distance of 5 pile diameters. Figure 7(b) shows the variation of void ratio against the distance to the centerline of the pile for a horizontal section B at a depth of 2.775 m from the ground surface (*see* Fig. 3), at the different stages of casing driving and pile compaction. The open markers show the results for the looser Case 1, while full markers illustrate the results for the initially denser Case 4. Case 1 becomes relatively more compacted when compared with other cases. At the end of the first stage the maximum void ratio reduction at this elevation was approximately 5.6% in Case 1 and 3.0% in Case 4. In this latter case, some dilatancy (increase of void ratio) for elements closer to the pile can be observed. Further densification is observed due to compaction of the sand/gravel layers introduced inside the pile. The gain during this stage was also more remarkable in Case 1. The maximum reduction in void ratio at

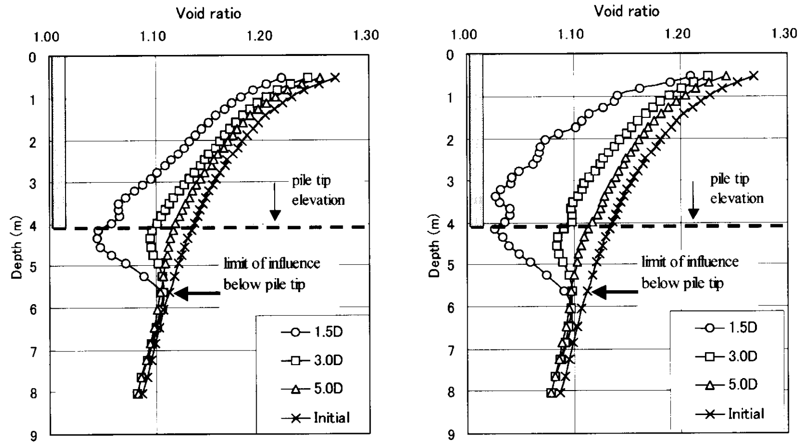

(a) End of Stage 1 (b) End of Stage 2

Fig. 6. Void ratio with depth at different distances from the pile, Case 1

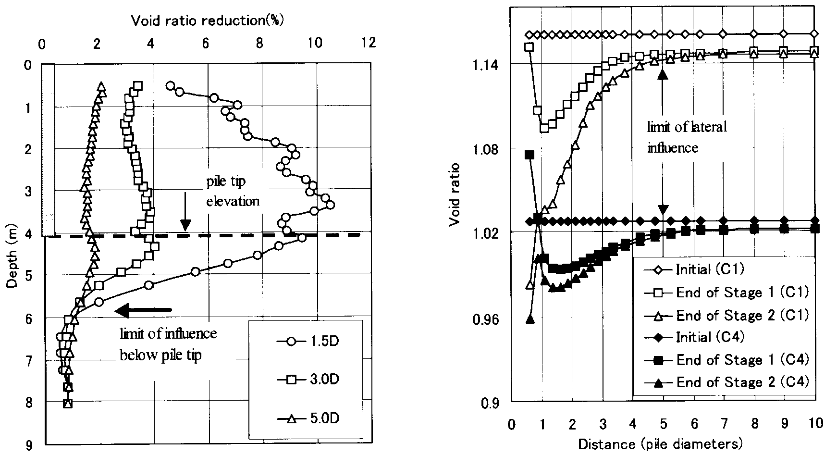

(a) Δe_R at the end of Stage 2 (Case 1) (b) Void ratios at the end of Stage 2 (Cases 1 & 4).

Fig. 7. Effect of densification in vertical and horizontal directions

section B was approximately 15% in the looser Case 1, 13% in Case 2, 11% in Case 3 and 6.5% in the denser Case 4. The extent of the densification also depends on the initial void ratio, but decreases steadily with distance from the centerline of the pile. There is an inflection point in this trend, which was roughly at a distance of 1.50 m (or 5 pile diameters -5*D*) from the centerline of the pile. Further than this point the void ratio reduction is rather small.

Stress Changes

It is important to analyse the effect of sand pile compaction on the distribution of horizontal and vertical stresses. The situation at the end of Stage 1 is shown in Figs. 8 and 9 for the looser Case 1. Figures 8(a) and (b) show, respectively, the distribution of horizontal (σ_h) and vertical stress (σ_v) at different distances from the pile centre at the end of the casing installation (Stage 1). It is interesting to note that both σ_h and σ_v increase significantly below the pile tip; however, along the pile length, the horizontal stresses increase, while the vertical stresses decrease keeping the mean stress (p) almost constant. The variation of the mean stresses (p) is shown in Fig. 9(a). When the pile is introduced below a certain level, the dense material that was at the tip dilates due to the shearing forces along the casing perimeter, undoing part of the previous densification. Therefore, the peak of mean stresses below the casing tip, shown in Fig. 9(a) for the pile driving stage, moves continuously downwards as the metal casing is inserted. This explains why the densification at end of Stage 1 is more localized under the pile tip, as shown in Fig. 6(a). At the same time, shearing due to casing installation, provokes a rotation of principal stresses, which results in horizontal stress increase and vertical stress decrease as shown in Fig. 8. The intense shearing can be appreciated in Fig. 9(b), which shows the steady increase of the principal stress ratio ($R=\sigma_1/\sigma_3$) at the end of the casing driving stage.

The stress distribution due to the construction and compaction of the sand pile is shown in Fig. 10, as well as

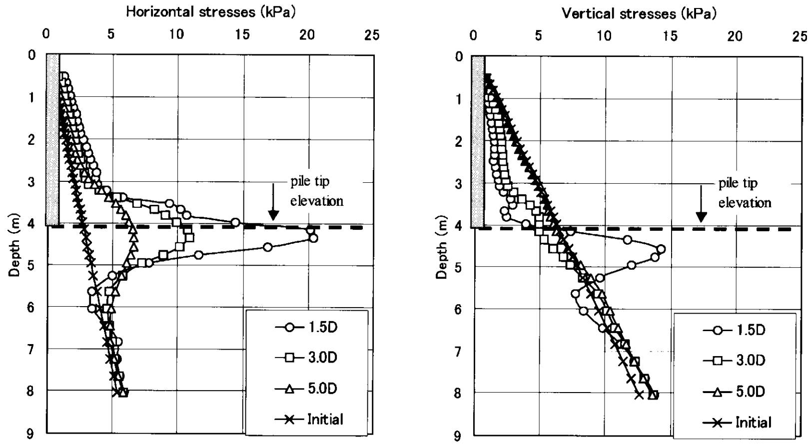

(a) Horizontal stresses σ_h.

(b) Vertical stresses σ_v.

Fig. 8. Stresses at end of Stage 1

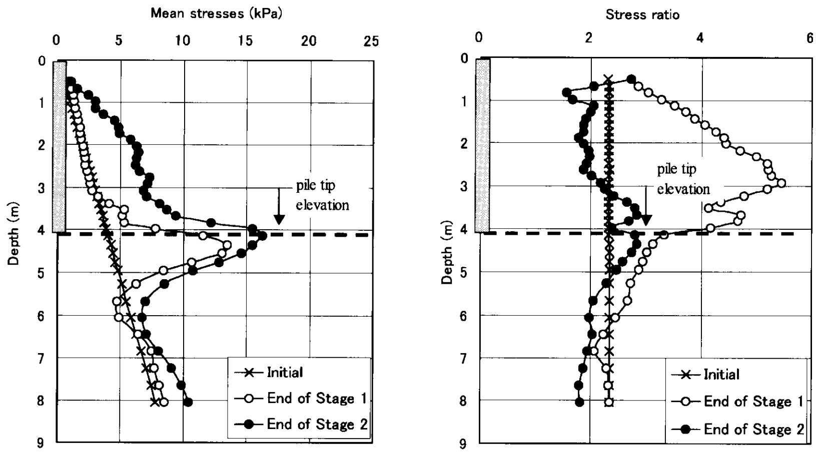

(a) Mean stresses

(b) Principal stress ratio

Fig. 9. Mean stresses and principal stress ratio at a distance of 1.5 diameters from pile center

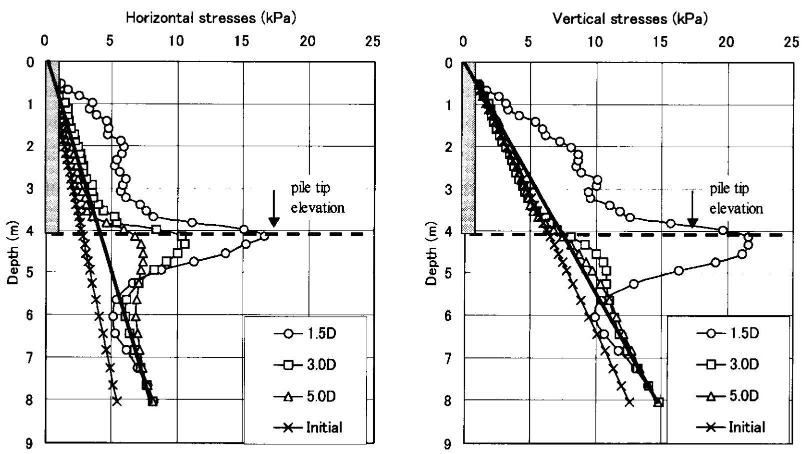

(a) Horizontal stresses σ_h (kPa)

(b) Vertical stresses σ_v (kPa)

Fig. 10. Stresses at end of Stage 2

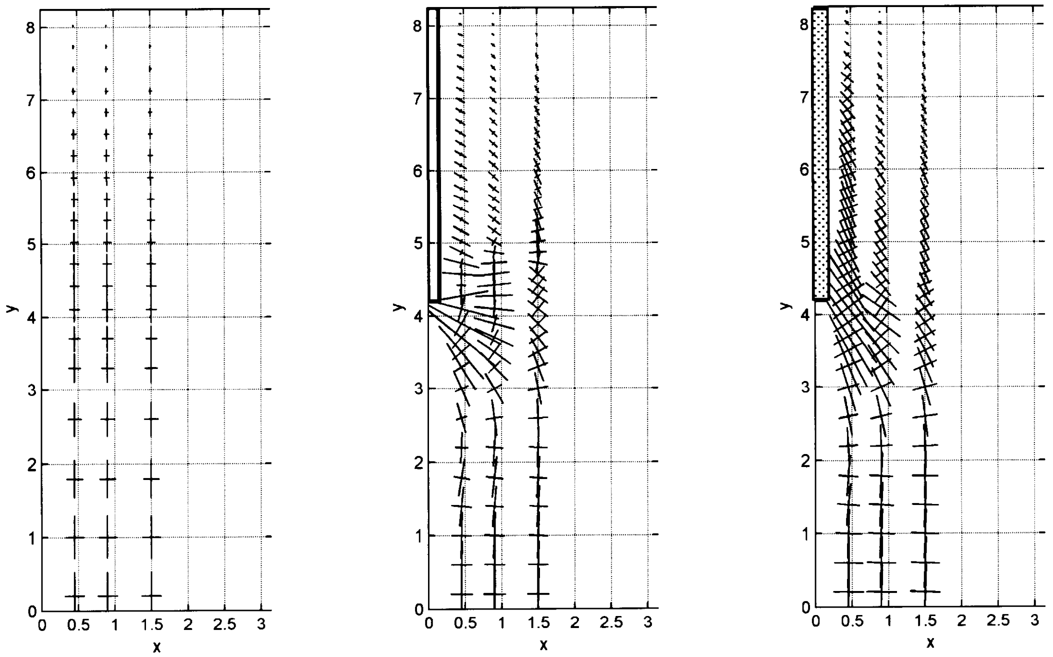

(a) Initial (b) After casing driving (c) Final condition

Fig. 11. Principal stresses, Case 1

in Fig. 9. It is possible to note that in Fig. 10 that there is a further increase in stresses below the pile tip, and increase of both horizontal and vertical stresses along the pile shaft. This is also shown by the increase in mean stress values and reduction of principal stress ratio in Fig. 9. This makes the densification process more uniform along the pile shaft, except at the superficial top layer (1.0 m), as also shown by the void ratio changes in Fig. 5(b). Below a certain depth of influence under the pile tip, it is interesting to note that the stresses follow a straight line, but more inclined than the initial geostatic line. Full lines without symbols representing these trends were drawn in Figs. 10(a) and (b) and extrapolated to the surface. The slope of the line on the vertical stress plot in Fig. 10(b) represents the new average unit weight of the sand deposit. The increase in vertical stress was around 17% at the bottom of the mesh (8.0 m depth). Along the pile shaft the effect of densification on the vertical stresses is only notable at a short distance from the pile centre, while the horizontal stresses spread further away.

The evolution of principal stresses is shown in Fig. 11 for Case 1, using the stresses crosses at the distances of 1.5, 3.0 and 5.0 pile diameters. The stress distribution at the initial state is shown in Fig. 11(a). The effect of casing installation is clearly shown in Fig. 11(b). Note that the direction of the major principal stress (σ_1) rotates towards the metal casing, becoming closer to the horizontal due to shearing. At the same time, the magnitude of the major principal stress (σ_1) increases along the tube length, while the minor principal stress (σ_3) decreases tending to the vertical, but keeping the mean stress approximately constant. The situation below the pile is slightly different with less rotation and higher magnitudes. Figure 11(c) shows the final situation after the construction of the sand compaction pile. Due to the compaction effect, the magnitude of the principal stress increases, at the same time that they rotate back as the direction of the major principal stress becomes more vertical again.

It is also important to analyse the combined effect of horizontal and vertical stress changes in the coefficient of lateral earth pressure ($K=\sigma_h/\sigma_v$), as shown in Fig. 12. During the metal casing installation, the shearing forces cause principal stress rotation with an increase in σ_h and a decrease in σ_v, as discussed previously. Therefore, there is a sharp increase in lateral stress ratio ($K=\sigma_h/\sigma_v$), as shown Fig. 12(a). At the end of the casing driving stage, the lateral stress ratio is rather uniform along the pile shaft, with some peak below the pile tip. However, it is interesting to note the situation after the construction of the sand compaction pile as shown in Fig. 12(b). There is still a sharp increase at some depth below the pile tip, but closer to the pile (1.5D), the value of K increases from the pile tip towards the ground surface along the pile length until a depth of about 0.5 m. This can be explained by the fact that the horizontal stresses increased relatively more than the vertical stresses during the sand pile compaction process.

EXPERIMENTAL INVESTIGATION

Well controlled in-situ tests on a loose sand deposit were carried out before and after ground improvement with sand-gravel compaction piles at the experimental site

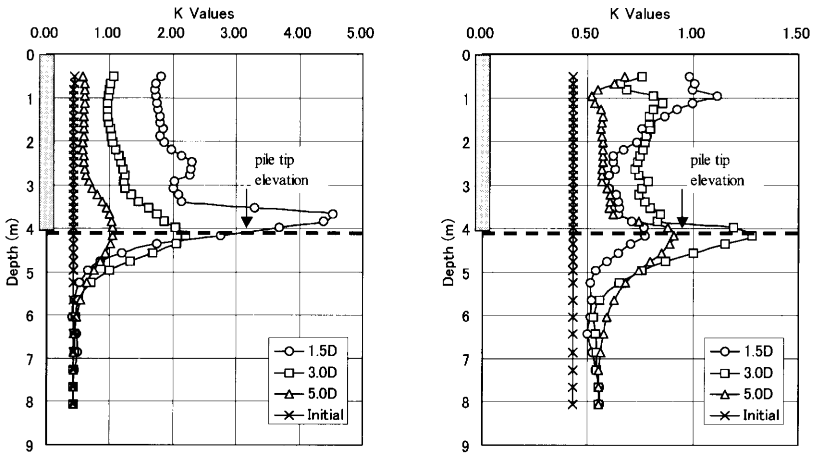

(a) At end of stage 1

(b) At end of stage 2

Fig. 12. Coefficient of lateral pressure $K=\sigma_h/\sigma_v$

of the University of Brasilia, Brazil, as part of a PhD research (Passos et al., 2004). The typical soil of the experimental site is a porous lateritic clay. Therefore, an artificial sand deposit had to be constructed in-situ for this research. This allowed full soil characterization and control of the deposit characteristics, besides careful installation of monitoring devices. Initially a trench 1.50 m wide, 3.0 m long and 2.5 m deep was excavated. Then the trench was filled with loose sand by pluviation using a wooden box (1.5 m × 0.5 m × 0.5 m) with a perforated bottom and a movable bottom window. The box had wheels, which could slide on tracks installed alongside the trench, 3.5 m above the excavation bottom. The sand was dried in the open air and sieved in a 2 mm mesh, before filling the wooden box. Then the bottom window was opened and the box slid along the trench to promote a sand rain, thus forming a loose sand deposition. The process was repeated in layers until the surface level was achieved.

A total of 15 sand piles with different configurations were planned. So far three piles were executed and tested. The construction method followed exactly the current practice, but a reduced pile diameter was adopted to conform to the trench dimensions. A metal casing with 10 cm of diameter was driven into the ground to a depth of 2.0 m, using a SPT tripod and a 50 kgf (0.5 kN) hammer. The sand-gravel mixture was compacted inside the casing with the hammer falling from 0.5 m, for a given number of blows such as to compact the material with Normal Proctor energy.

The results of some of these tests are presented and discussed in reference to the previous numerical analyses. It is emphasized, however, that the geometrical conditions, materials and initial states are not the same and any comparison should only be qualitative. The numerical analyses were class A predictions of real cases and are reproduced here not with the intention of back analyzing the field results, which were obtained from reduced scale in-situ models. On the contrary, the intention is to check the ability of the model in reproducing the basic mechanisms that occur in the field during sand compaction pile construction.

In-situ Test Program

The deposit was formed in horizontal layers by sand pluviation. The sand was dried in the open air and its moisture content was only hygroscopic (less than 1%). No water table is found at the site where the deposit was constructed. The unit weight γ of each layer of approximately 30 cm of sand was measured, using cylinders of known volume. Three measures at different points in the longitudinal direction of the trench were obtained for each layer. The properties of the deposit varied almost linearly with depth. Void ratios are higher at the surface ($e=0.87$ at $y=0.4$ m) and decrease with depth due to self weight ($e=0.67$ at $y=2.5$ m), as simulated in the numerical analysis (*see* Fig. 3(b)). Mean values were $\gamma_d=15.0$ kN/m^3 for the dry unit weight, void ratio of $e=0.78$ and relative density of $D_r=34\%$, thus achieving an initially loose state desired for this research. Minimum relative density was 5% at a depth of 0.4 m and maximum was 69% at 2.5 m.

The following in-situ tests were carried out on the ground before improvement: Standard Penetration Test (SPT), Dynamic Probing Light (DPL), Cone Penetration Test (CPT), Dilatometer Test (DMT) and Load Plate Test (LPT). In order to evaluate ground improvement due to a group of two sand-gravel piles, five DPL tests and two dilatometer (DMT) tests were performed after ground densification. Figure 13 shows a section and a plan view with the relative location of the tests after ground improvement. Details of test results can be found in Passos et al. (2004).

The Flat Dilatometer Test (DMT)

The dilatometer, illustrated in Fig. 14, consists of a steel blade measuring 220 mm in length, 95 mm in width and 14 mm in thickness. Its tip has a cutting edge at an

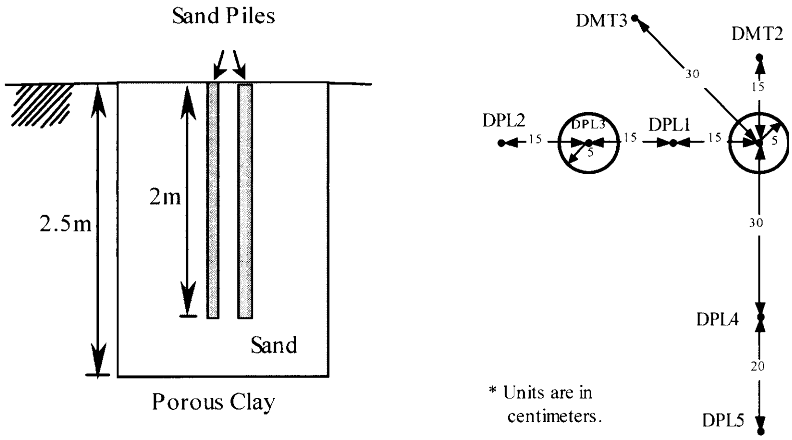

Fig. 13. Location of DPL and DMT tests for the groups of the two piles

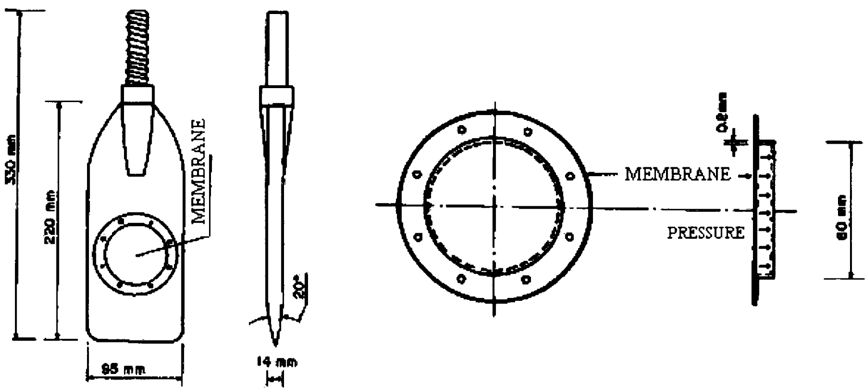

Fig. 14. Detail of dilatometer apparatus (Marchetti, 1985)

angle of 20°. One face of the apparatus has a circular metal membrane with 60 mm in diameter (Marchetti, 1985). This membrane expands under pressure during the test due to the introduction of nitrogen gas. The blade is attached to extension tubes and connected to a control unit in the ground surface. The apparatus is continuously driven into the ground with a hydraulic system at a rate of 2 cm/s.

The blade introduction is stopped at every 20 cm to perform the expansion test. Two readings are registered: P_0 corresponding to the pressure when the membrane is at rest; and P_1, which is the pressure necessary to displace the membrane by 1.5 mm outwards. These readings are then used to determine the following intermediary dilatometer test parameters: I_D (material index), E_D (dilatometer modulus) and K_D (horizontal stress index). These are computed as follows (Marchetti, 1997):

$$I_D = \frac{P_1 - P_0}{u_0} \tag{13}$$

$$K_D = \frac{P_0 - u_0}{\sigma'_{vo}} \tag{14}$$

$$E_D = 34.7(P_1 - P_0) \tag{15}$$

where u_0 = pre-insertion pore pressure; σ'_{vo} = pre-insertion effective overburden stress.

The dilatometer test parameters (I_D, E_D and K_D) are used to estimate geotechnical parameters by means of empirical correlations proposed in the literature for different materials (Marchetti, 1985). At the site of the tests performed during this research, the water table is not present ($u_0 = 0$).

The vertical stresses before ground improvement were computed using the unit weights measured during the sand deposition. For the porous clay between of 2.5 m and 4.5 m of depth, the average unit weight value is around $\gamma = 15$ kN/m^3. The unit weights after compaction were estimated from the initial values, assuming a uniform increase of 5%.

Figures 15(a) and (b) show, respectively, the values of the horizontal pressures P_0 and P_1, for the dilatometer tests performed after ground improvement in the points shown in Fig. 13. The results show considerable increase in the values of P_0 and P_1 till a depth of 2.3 m. This consequently reflects in the increase of dilatometer parameters shown in Fig. 16. These results show that ground improvement extends not only laterally, but also below the sand compaction pile tip, which was established at a depth of 2.0 m, while the loose sand deposit

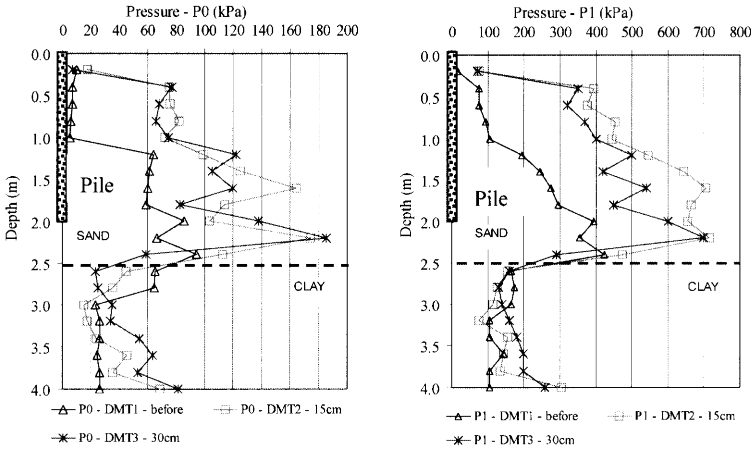

Fig. 15. Corrected pressures from DMT tests: P_0 and P_1

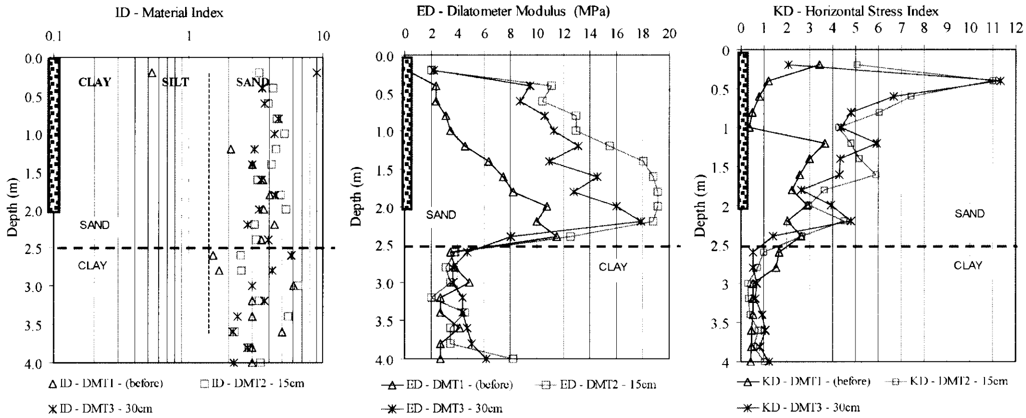

Fig. 16. DMT parameters: I_D-material index, E_D-dilatometer modulus and K_D-horizontal stress index

extended to the limit of the natural clay at a depth of 2.5 m. This is in good qualitative agreement with the results of the numerical predictions of Fig. 5, which show a significant decrease in void ratio down to about five pile diameters below the pile tip.

In the domain of the sand deposit between the depths of 0.40 m and 2.2 m, the curves for the horizontal stresses P_0 and P_1 after ground improvement are almost parallel to those before the improvement, thus indicating a rather uniform densification along the pile length, except for the more superficial layer, as also forecasted in the numerical analyses. For the position of DMT2 (15 cm or 1.5*D* from the pile center), the value of P_0 increased on average 65 kPa and P_1 increased about 350 kPa. Further away (30 cm or 3 pile diameters) the increase in these values is smaller but still very significant and rather constant, considering the natural variability of this kind of in-situ test. These results support the idea that the influence of sand piles tends to spread further in the horizontal direction than in the vertical as also predicted in the numerical analyses.

The transition between the artificial sand deposit and the original clay material is clearly identified by most dilatometer indices at a depth of 2.5 m, which corresponds to the bottom of the trench. It is striking that the material index (I_D) in Fig. 16(a) classifies the original clay ground as sand. This is because, this index identifies the material behavior rather than the material texture. Lateritic clays are generally formed of flocculated clay grains and behave rather like granular materials (Camapum de Carvalho et al., 1998). The porous clay deposit in the test site is unsaturated and it has been fully characterized by Marques et al. (2004) using different types of in-situ tests, including DMT. Correlations for geotechnical properties of unsaturated residual soils using dilatometer test have been proposed by several others, such as Cruz et al. (2004).

The increase in stiffness, shown by the variation of the dilatometer modulus E_D in Fig. 16(b), follows the same pattern of the mean stresses in Fig. 9(a). The increase is rather uniform along the pile length with a maximum value below the pile tip.

The lateral pressures measured with the dilatometer are shown in Fig. 16(c). A sharp increase in K_D was observed for the superficial ground until 1.0 m of depth. This is believed to be due to the lack of confinement at surface level. From this point it decreases steadily towards the pile tip. For deeper ground, until 2.3 m meters, sig-

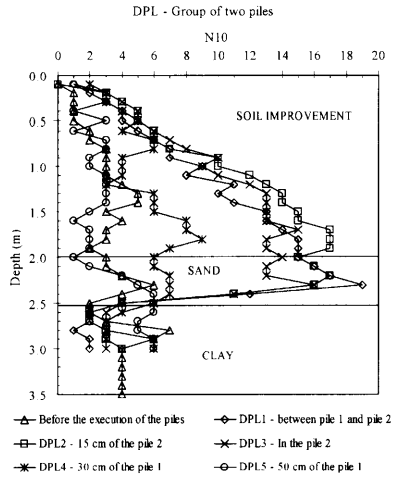

Fig. 17. DPL tests for the group of two piles

nificant increase in K_D can also be observed, but to a lesser extent than at the surface. These results follow the numerical predictions of Fig. 12(b) for a distance of 1.5*D* from the pile center.

Dynamic Probing Light (DPL)

Dynamic probing is mainly used in cohesionless soils. The expression "probing" is used to indicate that a continuous record is obtained from the test in contrast to, for example, the Standard Penetration Test (SPT). The aim of dynamic probing is to measure the effort required to drive a cone through the soil and to obtain resistance values, which correspond to the mechanical behavior of the soil.

A hammer of mass $M=10$ kg and a height of fall $H=0.5$ m is used to drive a conical pointed probe. The hammer strikes an anvil, which is rigidly attached to extension rods. The penetration resistance is defined as the number of blows (N_{10}) required for the probe to penetrate a defined distance (10 cm). DPL results are presented in diagrams, which show the N_{10} values on the horizontal axis and the depth on the vertical axis.

Figure 17 shows the results of DPL tests for the group of two piles. The results in this figure show an impressive gain in penetration resistance at DPL2 (15 cm or 1.5*D* from the center of pile 2 as shown in Fig. 13), followed by a still significant gain in DPL 4 (30 cm or 3.0*D* from the center of pile 1) and no gain in DPL5 (50 cm or 5.0*D* from the center of pile 1). These results are consistent with the numerical predictions presented in Fig. 7.

The results in DPL1, 15 cm from the two piles centers are basically equal to those in DPL2 (also 15 cm from a pile of pile 2, but in opposite direction of pile 1 as shown in Fig. 13). This shows that no improvement is obtained when the ground is already dense, due to the construction of the first pile. Therefore, there is no superposition of improvement between the two piles. It is even possible that, on very dense ground, the sand compaction pile construction might have a negative impact, due to soil positive dilatancy (volumetric increase). In this case the final ground condition might become looser than its initial state and the pile construction would have an adverse effect, instead of densification.

Another interesting result is that of DPL3, which was performed right in the center of pile 2, after all other tests had finished. The results show that the penetration resistance inside the sand-gravel pile is basically the same as that around the improved sandy soil (DPL2). This may be related to the dilatancy of the compacted material inside the metal casing due to shearing as the casing is pulled out. This result is still preliminary and further investigation is needed. Pile loading tests and plate loading tests on the improved ground are programmed. If the deformation properties of the pile and surrounding soil are similar, this could be of significant practical importance for designers. It could indicate that the foundation should be treated as a simple footing over improved ground instead of a piled raft.

CONCLUSIONS

Numerical analyses and field study with in-situ testing were carried out for the compaction of ground using sand pile. The numerical analyses used subloading t_{ij} model. In-situ tests included Dynamic Probing Light (DPL) and Dilatometer (DMT) tests before and after ground improvement. The main conclusions are as follows:

The looser the initial soil conditions, the more effective is the densification process. This is clear from the numerical simulations for a single pile and from the results of dynamic probing tests (DPL), which showed significant gain of penetration resistance at a distance of 1.5 pile diameter for a single pile, but no additional gain at the same distance when a second pile was constructed. In originally dense regions or in regions highly compacted by the sand pile construction process, as well as in regions of low confinement, some dilatancy was observed.

The extent of the densification process also depends on the initial ground condition, but can be roughly estimated as encompassing a region, which extends about three diameters from the pile centerline and five diameters below the pile tip, for tests which measure primarily vertical resistance, such as DPL. However, the numerical analyses and the results of DMT tests indicate that the influence on the horizontal direction may extend further to about five pile diameters.

Metal casing installation and sand pile compaction contribute to ground densification. The first stage is more efficient to compact the region below the pile tip, although some lateral densification is also observed. During the second stage, the ground densification becomes more uniform around the pile. At superficial layers, the effect of compaction is not efficient due to the low confinement. Therefore, the numerical results and the in-situ tests give support to the common engineering practice of disregarding this layer to about 1.0 m when considering a shallow footing foundation.

The combination of DMT and DPL tests gives a good overall picture of the densification process, since the soil is loaded in different directions in each test. Further insight can be gained with the help of numerical analyses, but for that purpose it is of vital importance to adopt a constitutive model, which can appropriately account for the soil densification, such as subloading t_{ij} model of Nakai and Hinokio (2003, 2004).

DPL tests performed in the sand-gravel pile itself indicated resistance level compatible with those of the improved ground around the pile. Further investigation is needed in relation to the deformation properties of the pile and the surrounding soil. If they also happen to be similar, this could indicate that shallow foundations over this soil should be designed as simple footings over improved ground, instead of piled rafts.

The consideration of large strains and the pile dynamic penetration effects remain to be studied in future numerical analyses.

ACKNOWLEDGMENTS

The authors acknowledge the financial support of the Brazilian National Research Council (CNPq) and the Japanese Ministry of Education, Science and Culture. The first author is particularly indebted to the Venture and Business Laboratory (VBL) of Nagoya Institute of Technology (NIT), which made possible this joint research between the Geotechnical Groups of NIT and the University of Brasilia (UnB).

REFERENCES

1) Asaoka, A., Kodaka, T. and Nozu, M. (1994): Undrained shear strength of clay improved with sand compaction piles, *Soils and Foundations*, **34** (4), 23–32.
2) Camapum de Carvalho, J., Farias, M. M. and Araki, M. S. (1998): Relation between microstructure and collapse in Brasilia's Porous Clay, *IS-TOHOKU'98—Int. Symp. Problematic Soils*, Sendai, Japan.
3) Chowdhury, E. Q. and Nakai, T. (1998): Consequences of the t_{ij}-concept and a new modeling approach, *Computer and Geotechnics*, **23**, 131–164.
4) Cruz, N., Viana da Fonseca, A. and Neves, E. (2004): Evaluation of effective cohesive intercept on residual soils by DMT and CPT, *Proc. ISC'2 Int. Site Characterization*, Porto, Portugal, 1275–1278.
5) Dafalias, Y. F. and Popov, E. P. (1975): A model of nonlinearly hardening materials for complex loading, *Acta Mechanica*, **21**, 173–192.
6) Farias, M. M., Nakai, T., Hinokio, M., Shahin, H. M. and Pedroso, D. M. (2003): Prediction of the densification process of compacted sand piles using sub-loading t_{ij} model, *Proc. Int. Workshop on Prediction and Simulation Methods in Geomechanics*, Athens, Greece, 185–188.
7) Gusmão Filho, J. A. (1995): Contribution to the practice of foundations: the experience of Recife, *Thesis*, Federal University of Pernambuco (in Portuguese).
8) Hashiguchi, K. (1980): Constitutive equation of elastoplastic materials with elasto-plastic transition, *J. Appl. Mech.*, ASME, **102** (2), 266–272.
9) Ichimoto, E. and Suematsu, N. (1981): Sand compaction pile method, *Tsuchi-to-Kiso*, JSSMFE, **29** (5), 13–20 (in Japanese).
10) Lambe, T. W. (1973): Up-to-date methods for investigating the strength and deformability of soils, *Proc. 8th ICSMFE*, **3**, 1–43.
11) Marchetti, S. (1985): On the field determination of K_0 in sand, *Discussion Session No. 2A, Proc. XI ICSMFE*, S. Francisco, **5**, 2667–2673.
12) Marchetti, S. (1997): The flat dilatometer: design applications, *Third Geotech. Engrg. Conf.*, Cairo University, Keynote Lecture, 26.
13) Marques, F. E. R., Almeida e Sousa, J., Santos, C. B., Assis, A. P. and Cunha, R. P. (2004): In situ characterization of the Brasilia porous clay, *Proc. ISC'2 Int. Site Characterization*, Porto, Portugal, 1301–1310.
14) Matsuoka, H. and Nakai, T. (1974): Stress-deformation and strength characteristics of soil under three different principal stresses, *Proc. JSCE 232*, 59–70.
15) Miyata, M., Nakai, T., Hinokio, M. and Murakami, K. (2003): Numerical analysis for localized deformation of clay based on infinitesimal and finite deformation theory, *J. Appl. Mech. JSCE*, Japan, **6**, 455–465.
16) Nakai, T. (1989): An isotropic hardening elastoplastic model for sand considering the stress path dependency in three-dimensional stresses, *Soils and Foundations*, **29** (1), 119–137.
17) Nakai, T. and Hinokio, M. (2003): An isotropic hardening model for normally and overconsolidated soils with t_{ij} concept and subloading surface concept, *Proc. 1st Int. Workshop on New Frontiers in Comp. Geotech.*, Calgary, 3–16.
18) Nakai, T. and Hinokio, M. (2004): A simple model for normally and overconsolidated soils with unified material parameters, *Soils and Foundations*, **44** (2), 53–70.
19) Nakai, T. and Matsuoka, H. (1983): Shear behaviors of sand and clay under three-dimensional condition, *Soils and Foundations*, **23** (2), 26–42.
20) Nakai, T. and Matsuoka, H. (1986): A generalized elastoplastic constitutive model for clay in three-dimensional stresses, *Soils and Foundations*, **26** (3), 81–98.
21) Nakai, T. and Mihara, Y. (1984): A new mechanical quantity for soils and its application to elastoplastic constitutive models, *Soils and Foundations*, **24** (2), 82–94.
22) Neely, W. J. (1990): Bearing capacity of expanded-base piles in sand, *ASCE J. Geotech. Engrg.*, **116** (1), 73–87.
23) Okamura, M., Ishihara, M. and Oshita, T. (2003): Liquefaction resistance of sand deposit improved with sand compaction piles, *Soils and Foundations*, **43** (5), 175–187.
24) Passos, P. G. O., Farias, M. M. and Cunha, R. P. (2004): Use of DMT and DPL tests to evaluate ground improvement in sand deposits, *Proc. ISC'2 Int. Site Characterization*, Porto, Portugal, 1709–1716.
25) Pedroso, D. M. (2002): Elastoplastic models for clayey soils: Behavior forecasting capacity and integration of constitutive relations, *MSc. Thesis*, University of Brasilia, Brazil (in Portuguese).
26) Pedroso, D. M. and Farias, M. M. (2003): Comparison between Cam-clay and t_{ij}-clay elastoplastic models for the simulation of the mechanical behavior of clays under three-dimensional stress states, *Proc. 12th Panamerican Conference on SMGE*, USA.